Wide bandgap halide perovskite absorbers for semi-transparent photovoltaics: from theoretical design to modules

Fabio Matteocci[1, #], Daniele Rossi[1, #], Luigi Angelo Castriotta[1], Daniel Ory[2,3], Salim Mejaouri[2,3], Matthias Auf der Maur[1], Frédéric Sauvage[4], Stefania Cacovich[5] and Aldo Di Carlo[1,6] *

[1]CHOSE (Centre for Hybrid and Organic Solar Energy), Department of Electronic Engineering, University of Rome "Tor Vergata", 00133, Rome, Italy

[2]Institut Photovoltaïque d'Île-de-France (IPVF), 18 Boulevard Thomas Gobert, Palaiseau, 91120, France

[3]Électricité de France (EDF), R&D, 18 Boulevard Thomas Gobert, Palaiseau, 91120, France

[4]Laboratoire de Réactivité et Chimie des Solides, CNRS UMR7314, Université de Picardie Jules Verne, Hub de l'énergie, 15 rue Baudelocque, 80039 Amiens, France

[5]CNRS, École Polytechnique, IPVF, UMR 9006, 18, Boulevard Thomas Gobert, 91120 Palaiseau, France

[6]ISM-CNR, Istituto di Struttura della Materia, Consiglio Nazionale delle Ricerche, Roma, 00133 Roma (Italy)

[#]These authors contributed equally

[*]Corresponding Author: aldo.dicarlo@uniroma2.it

Abstract

The interest in Building Integrated Photovoltaic (BIPV) is growing worldwide. A pivotal role in the development of these technologies can be played by semi-transparent perovskite solar cells (ST-PSCs), thanks to their excellent potential in terms of both Average Visible Transmittance (AVT) and

color neutrality. Here, we demonstrate that $MAPb(Br_{1-x}Cl_x)_3$ wide band gap perovskite thin films allow to fabricate efficient and semi-transparent solar cells and modules. To this purpose, electro-optical simulations were employed to optimize the device stack by considering the transmitted/reflected light at each interface between the constituent layers, the composition and the thickness of the perovskite absorber and the impact of the transparent top contact. By combining theoretical and experimental results, we show that the optimal perovskite composition corresponds to a chloride molar ratio equal to 0.13, resulting in a champion device efficiency of 6.3%, Average Visible Transmittance of 69.4% and Light Utilization Efficiency of 4.37%. Furthermore, semi-transparent perovskite mini-modules with a stabilized efficiency of 5.45% and AVT of 59.4% with an aperture area of 53.6 cm^2 were fabricated defining a new state-of-art for semi-transparent modules. We thus demonstrated efficient and highly semi-transparent perovskite solar modules for the development of PV windows, paving the way for their future integration in architectural components.

Introduction

Photovoltaics (PV) represents one of the crucial research fields to meet the growing worldwide energy demand of electricity generated from innovative and cost-effective renewable sources[1, 2]. Several issues are related to the extensive use of terrestrial PV such as the high maintenance/distribution costs, the storage and the land cover requirement[3]. In this scenario, the research on Building Integrated Photovoltaics (BIPV) field is crucial to explore solutions for Nearly Zero Emission and Positive Energy Buildings oriented to design micro-hub-like buildings capable to harvest, store and supply energy[4]. In this context, the use of transparent (in the visible range) PV could lead to a deep integration in building façade and windows. Although transparent BIPV technologies based on spatially segmented opaque PV like c-Si and Copper Indium Gallium Selenide (CIGS) are now commercially available, they do not meet the aesthetical and transparency requirements for PV glass façade integration[5]. Over the years, visible transparent PV (TPV) with emergent technologies such

Organic Solar Cells [6-9] and Dye Sensitized Solar Cell (DSSC)[10-14] has been demonstrated for their use in BIPV even though the quite low overall performance in terms of Average Visible Transmittance (AVT) and power conversion efficiency (PCE) limited their exploitation to market level. Recently, perovskite solar cells (PSCs) have attracted great interest in the PV field showing record PCE of 25.5%[15] for single-junction and up to 29.1% for PSC/c-Si tandem[16] architecture. These important achievements have been obtained by using a perovskite formulation based on a specific mixture of iodide/bromide precursors with a panchromatic absorption in the visible spectrum and optical band gap in the range of 1.5-1.7 eV[17-21]. However, the composition of perovskite is quite tenable and compositions with large band gap can be developed by varying the halide nature and composition, permitting the realization of semi-transparent PSCs[22]. Several approaches have been reported for the realizations of semi-transparent PSCs based on the reduction of the perovskite thickness[23-25], the perovskite coverage[26, 27] and the increase of the optical band gap[28]. The first two approaches are mainly based on the development of a colour neutral PSC device with the aim to decrease the panchromatic absorption in the visible light spectrum[29]. This resulted in quite low AVT values (10-20%) with PCE less than 15%[25]. A different approach to the problem relies on the wide band gap halide perovskite materials based on iodide-bromide (I^-/Br^-)[25, 30], pure bromide (Br^-) [31-33] or bromide-chloride (Br^-/Cl^-) halide compositions [34, 35]. In this scenario, an emergent class of Br^-/Cl^- perovskites with general formula $MAPb(Br_{1-x}Cl_x)_3$ and $FAPb(Br_{1-x}Cl_x)_3$ has been developed showing AVT > 50% and PCE > 7.5%[34].

To compare the different combinations of PCE and AVT in TPV an important metric has been introduced by Traverse at al., the Light Utilization Efficiency (LUE), defined as the product between the PCE and the AVT.[5] It represents an overall system efficiency that links the PCE performance together with the AVT of the device stack.

One of the critical topic in the design of TPV is the optical management comprising the control of the visible light absorption in the active material and the light reflections at each interface of the device

stack. Indeed, reflection and interference phenomena will highly affect the AVT value of the device. Therefore, the development and use of simulation tools is highly demanded to find out possible strategies to maximize AVT and PCE of TPV. In this paper, we report the results on theoretical/experimental approach to guide the design of highly transparent PSC (ST-PSC) using $MAPb(Br_{1-x}Cl_x)_3$ perovskite with specific chloride molar ratio (x_{Cl} = 0, 0.04, 0.13, 0.2, 0.26). This combined approach has allowed to achieve state-of-art PCE = 7.9% (AVT = 56.9%) and state of art values AVT = 69.7% (PCE = 6.3%) by varying the x_{Cl} concentration from 0 to 0.13. Furthermore, we report promising results about the light/thermal stability of the ST-PSC following accelerated stability test and the first demonstration of semi-transparent perovskite solar modules (ST-PSM) with PCE greater than 7% and 5.5% on active area of 10.3 cm^2 and 48.8 cm^2, respectively, with AVT greater than 50%.

Results and discussion

To design the ST-PSCs we make use of fine-tuned electro-optical simulations where a combination of experimental characterizations of material/devices and literature data permitted to identify all the relevant simulation parameters. In particular, we determined the optical properties of $MAPb(Br_{1-x}Cl_x)_3$, such as the absorption coefficient and energy gap, to assess the impact of Cl addition on the AVT and PCE of ST-PSCs.

In **Figure 1a**, we show the absorption coefficient spectra determined from the absorbance measurements performed on 500 nm-thick $MAPb(Br_{1-x}Cl_x)_3$ perovskite films with increased x_{Cl} molar ratios (0, 0.04, 0.13, 0.20, 0.26). The absorption spectra exhibit a clear excitonic contribution that we fitted according to the Elliott model[36, 37] with the contribution of a continuous part and an excitonic part (See SI for further information). The exciton binding energy was found equal to about 30 meV and rather independent on x_{Cl}, although slightly higher for lower values of x_{Cl}. Whereas the amplitude of the excitonic part increases also with x_{Cl} content, it tends to slightly diminish compared to the continuous part for higher values of x_{Cl}. The bandgap energy increases linearly with x_{Cl} values from

2.39 eV for $x_{Cl} = 0$, in agreement with the values reported by Mariano et al. [38] and Chen et al. [39], to 2.56 eV for $x_{Cl} = 0.26$ (**Figure 1b**). XRD characterization of the different films was carried out to evaluate the structural evolution upon addition of chloride into the perovskite structure. Regardless of the chloride concentration in $MAPb(Br_{1-x}Cl_x)_3$, the latter crystallized into a cubic structure with Pm-3m space group. All films are highly textured, which translates into a strong preferential orientation along (001) planes (**Figure S1a**). The peaks position are continuously shifting to higher 2θ angles by increasing the x_{Cl} molar ratio (**Figure 1c**). The evolution of the lattice cell parameters has been refined using Fullprof software. The linear decrease of the lattice cell parameters upon addition of chloride verifies Vegard's law, thus confirming the solid solution domain in $MAPb(Br_{1-x}Cl_x)_3$ between $0 < x < 0.26$ (**Figure S1b**) [31]. In this range of chloride concentration, the lattice shrinks from a = 5.9413(4) Å to a = 5.8657(2) Å. The film's morphology (see SEM images in **Figure S2**) is not affected by the chloride addition. It shows a network of melted perovskite crystals resulting by the methylamine gas post-treatment. This confirms the defect healing of $MAPbBr_3$ perovskite after recrystallization induced by the methylamine gas post-treatment [40]. The cross-section of the device stack ($FTO/c\text{-}TiO_2/m\text{-}TiO_2/perovskite/PTAA/ITO$) for x_{Cl} = 0, 0.04 and 0.13 are investigated by HAADF STEM (High Angle Annular Dark Field – Scanning Transmission Electron Microscopy) characterization imaging and reported in **Figure 1e**. The results show a uniform thickness of the m-$TiO_2 + MAPb(Br_{1-x}Cl_x)_3$ layers being equal to 500 nm for all the compositions.
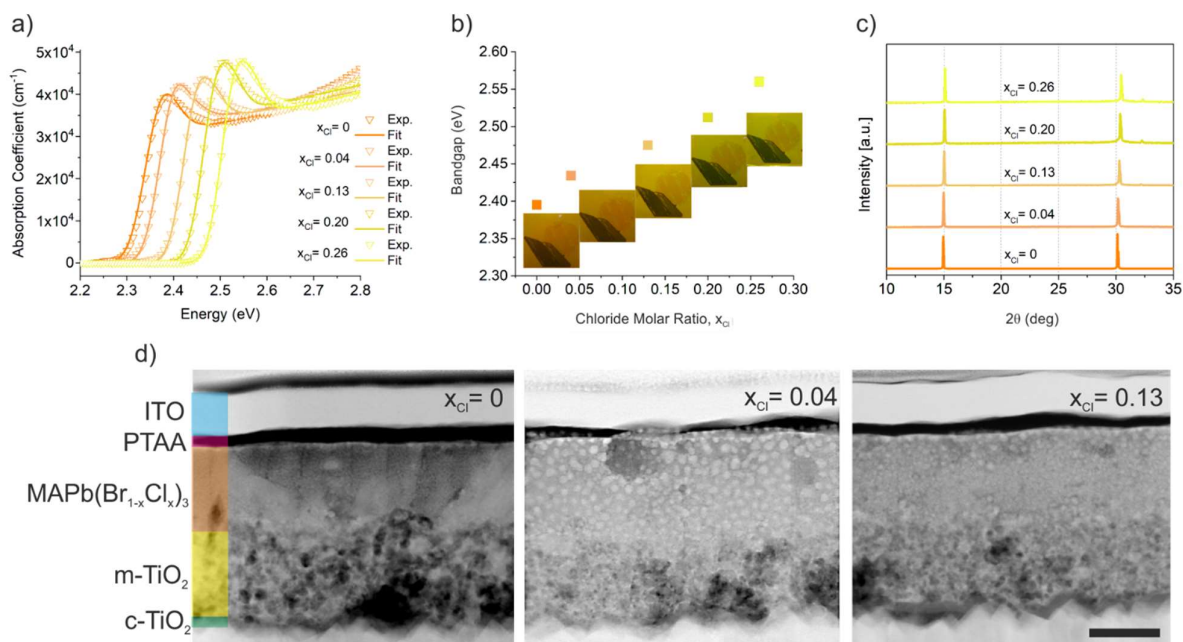
Figure 1. a) Absorption coefficient curves of the MAPb(Br$_{1-x}$Cl$_x$)$_3$ perovskite layer deposited on glass substrate, including fits of the excitonic contribution using the Elliott model; b) Energy bandgap variation extracted from Elliot model for x$_{Cl}$ = 0, 0.13, 0.2, 0.26. c) Evolution of the x-ray diffractogram collected on glass/MAPb(Br$_{1-x}$Cl$_x$)$_3$ samples with x$_{Cl}$ = 0, 0.13, 0.2, 0.26; d) Cross sectional HAADF STEM images of the device stack (FTO/c-TiO$_2$/m-TiO$_2$/MAPb(Br$_{1-x}$Cl$_x$)$_3$/PTAA/ITO) for x$_{Cl}$ = 0, 0.04 and 0.13. The scale bar is 200nm for all the images.

All the optical and morphological characterizations of both perovskite absorbers and full device stack serve as the basis for the electro-optical parametrization. Several data are needed to define electro-optical parametrization (reassumed in Tab S1-S2) such like the thickness, the extinction coefficient (k) and the refractive index of the layers forming the device stack including the electrodes, the electron and hole selective contacts (Figure S3a-f) and the perovskite absorber (Figure S4a-b).
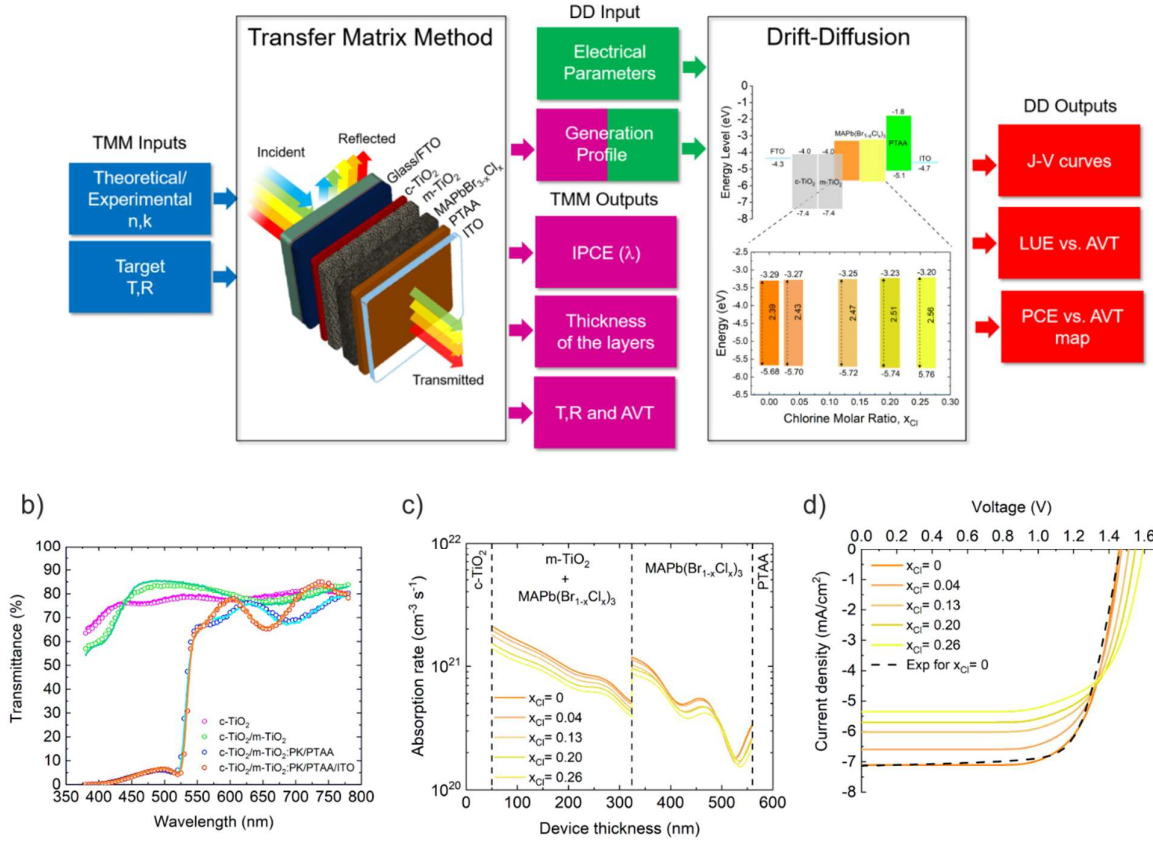
Figure 2. a) Block diagram describing the combined TMM/DD simulative approach used to determine the electro-optical performance of investigated devices. Blue and magenta blocks indicate respectively the inputs provided to the TMM based algorithm and corresponding optical outputs, while the green and red the inputs and outputs of the DD simulator. The magenta/green indicating the optical generation profile is used to couple the optical and electrical modeling. b) Theoretical/experimental comparison of transmittances starting from the commercial FTO on glass substrate, the partial stack up to the PTAA and full transparent device. c) The generation profiles obtained by varying the chloride molar ratios are used to draw the d) J-V characteristics by drift-diffusion simulations.

The block diagram shown in Figure 2a summarizes the electro-optical modeling: the optical calculations are performed by using a Transfer Matrix Method (TMM) based algorithm[41], while the charge transport is calculated using a drift-diffusion (DD) model[42] based simulation tool. The TMM allows to model the propagation of the incident solar radiation through the multi-layered solar cell structure, basing the calculations on the complex refractive index ($N=n_0 + ik$) of each device layer. Besides the estimation of the electromagnetic field confinement, TMM calculations were used

to confirm the thickness of each layer measured by STEM. This is done by an iterative mean square error (MSE) minimization process, which gradually reduces the difference between the theoretical and experimental transmittance/reflectance (T/R) spectra in the visible range of wavelengths (380-780 nm). The results are resumed in Figure 2b where the fitting process is performed after each layer deposition during the device fabrication of MAPbBr$_3$ (x_{Cl} = 0). In particular, the mesoporous layer containing TiO$_2$ nanoparticles and perovskite is modeled as a blend, for which the effective refractive index (n_0) and extinction coefficient (k) are described by effective medium approximation (EMA) approach[43], and the volume porosity (Φ) and pore-filling (PF) work as weight variable[40]. The results of the layer dimensions obtained with TMM and the comparison with STEM measurement (of some layers) are summarized in Table 1.

Table 1. Thicknesses obtained by MSE-minimization iterative TMM calculations for the reference device fabricated with MAPbBr$_3$. Φ indicates the volume porosity of the mesoporous TiO$_2$. Values reported in brackets are the averaged thicknesses extracted from HAADF STEM images.

Glass [mm]	SnO$_2$ [nm]	SiO$_2$ [nm]	FTO [nm]	c-TiO$_2$ [nm]	Φ_{m-TiO2} (%)	m-TiO$_2$ [nm]	MAPbBr$_3$ [nm]	PTAA [nm]	ITO [nm]
1.8	16	28	353	-	-	-	-	-	-
1.8	16	28	353	24	58.2	289	-	-	-
1.8	16	28	353	24	57.9	274	221	32	-
1.8	16	28	353	24	59.8	274	221	32	113
						(265±15)	(220±20)	(38±10)	(113±1.5)

Starting from the results for x_{Cl} = 0, we extended the theoretical calculation for MAPb(Br$_{1-x}$Cl$_x$)$_3$ perovskite composition with the aim to evaluate potential perovskite absorber able to guarantee an improved AVT without strongly penalizing the PCE. The coherent transmittance T(λ) and absorbance A(λ) were calculated by only varying the perovskite composition to determine the AVT, theoretical EQE and generation rate profile G(x) within the active layer. The resulting G(x) profile is then

included as input in DD model to guarantee the electro-optical coupling (Figure 2c). The DD

simulations were performed for $MAPb(Br_{1-x}Cl_x)_3$ compositions using G(x) and the electrical

parameters (Table S2) showing the resulting J-V characteristics depicted in Figure 2d and compared

with experimental results for $x_{Cl} = 0$. As expected from the increase of the perovskite band gap, the

Voc increase is related to the Jsc decrease by increasing the chloride molar ratio.

The AVT of full devices can be tuned by varying the ITO thickness. To this end, we performed

electro-optical simulations for each perovskite composition by varying the ITO thickness in the range

between 90-250 nm. This step aims to maximize the transmittance in the visible range above the

perovskite absorption cut-off wavelength ($\lambda_{cut-off}$), by exploiting the optical interference mechanisms

which is also related to the ITO thickness (t_{ITO}). Thus, an optimization of t_{ITO} allows to increase AVT

preserving or even slightly improving the PCE (drop in ITO sheet resistance). However, although

the design of the ITO electrode is mainly driven by the trade-off between its optical/electrical

properties (AVT and sheet resistance), the feasibility of the sputtering process when applied on full

device stacks and the sputtering-induced damage has to be considered[44].
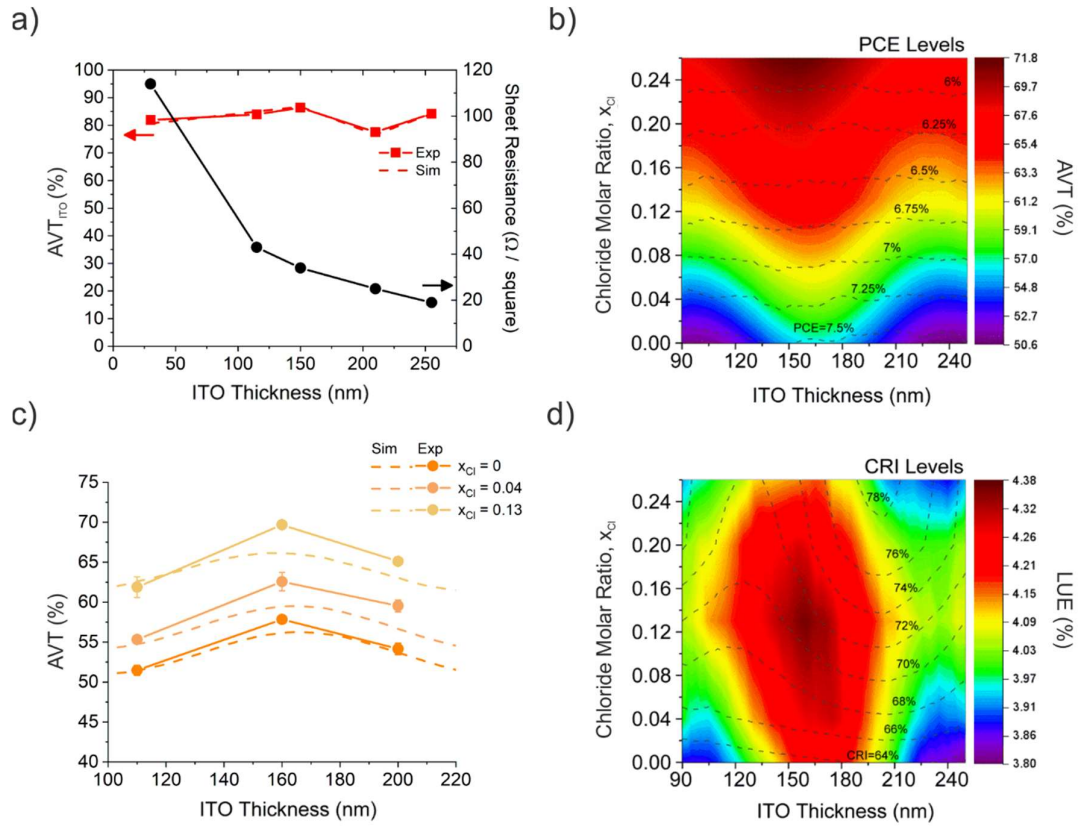
Figure 3. a) AVT and sheet resistance measured for different ITO thicknesses deposited on glass. b) Colored map indicates the dependence of the theoretical AVT varying the x_{Cl} and the t_{ITO}. The level curves indicate the predicted PCE values. c) Comparison of the AVT value obtained by the theoretical results and the averaged experimental results for x_{Cl} = 0, 0.04, 0.13. d) Colored map indicate the dependence of the theoretical LUE varying the x_{Cl} and the t_{ITO}. The level curves indicate the predicted Color Rendering Index (CRI).

To this end, different thickness of transparent ITO contacts were deposited on glass substrate by increasing the sputtering time using a low-temperature/low-power magnetron sputtering. The films were characterized by using the T/R and 4-point probe resistivity measurements. The good comparison between experimental T/R spectra and TMM simulation results for several sputtering time (**Figure S5a**) allows for a careful estimation of the ITO thickness and the AVT as shown in **Figure 3a**. The sheet resistance of ITO shows a clear decrease by increasing the t_{ITO} reaching 17 Ω/□ for 254nm and electrical resistivity equal to $5·10^{-5}$ Ω·m. TMM/DD calculations have been then performed considering the full stack of the device and varying ITO thickness and Chloride molar

ratio as reported in **Figure 3b** where we show the color map for AVT varying the x_{Cl} (0 - 0.26) and the t_{ITO} (90-250nm). The dashed level curves in black are corresponding to the PCE. The map clearly shows that the PCE is mainly controlled by the perovskite composition, while both the t_{ITO} and x_{Cl} are impacting on the AVT. This is well visible by analyzing the main factors affecting the AVT with respect to a specific range of wavelengths. For $\lambda < \lambda_{cut-off}$, the AVT is mostly affected by the absorption of the perovskite layer that is mainly dependent to its composition and thickness. On the other hand, for $\lambda > \lambda_{cut-off}$, the AVT is highly dependent to diffractive phenomena, that are more pronounced where the wavelength of the incident photons is comparable to the thickness of the layers constituting the device. In this scenario, the destructive/constructive interferences play a role on both the confined and outcoming electromagnetic field. Following the theoretical prediction, a batch of three devices were fabricated by varying the t_{ITO} (110nm, 160nm and 200nm) and the $MAPb(Br_{1-x}Cl_x)_3$ perovskite composition with x_{Cl} equal to 0, 0.04 and 0.13 and measuring the transmittance spectra (**Figure S5b-d**). For $\lambda > \lambda_{cut-off}$, the experimental results confirmed the role of diffractive phenomena on the transmittance spectra as predicted from the theoretical simulations. In **Figure 3c**, the impact of the t_{ITO} on the AVT is reported for both experimental data and theoretical results. As predicted by the simulations, a remarkable relative increase of the AVT for $t_{ITO} = 160nm$ (around +10% with respect to $t_{ITO} = 110nm$) is experimentally found for all the perovskite compositions.

The knowledge of PCE and AVT behaviors allows the theoretical calculation of the LUE by varying the x_{Cl} and the t_{ITO} as shown in color-map of **Figure 3d**. LUE can reach values over 4%, which represents the state-of-art limit achieved so far by TPV technologies[5]. The best LUE value being equal to 4.36 was obtained for $t_{ITO} = 160$ nm and $x_{Cl} = 0.13$ corresponding to a CRI equal to 71.2%. In **Figure S6**, we reported the CIE1931 diagram chromatic coordinates by varying the x_{Cl} in the $MAPb(Br_{1-x}Cl_x)_3$ perovskite composition. The results were obtained starting from experimental data. Based on the simulated AVT, PCE, LUE and CRI we outline that relatively low content of chloride ($x_{Cl} = 0.13$) in the $MAPb(Br_{1-x}Cl_x)_3$ perovskite composition represents the best trade-off between all

the key characteristics to be considered for the design of the ST-PSC. This work clearly evidences the advantages of introducing a low level of chloride into the perovskite and the results presented outperforms those obtained for pure bromide perovskite ($x_{Cl} = 0$). This is also visible in the steady-state photoluminescence (PL) of the different films showing a maximum of PL for $x_{Cl} = 0.13$. For higher x_{Cl}, a strong decrease of PL is observed suggesting the creation of non-radiative defects **(Figure S7a)**. At same time, the PL band shifts towards the blue in agreement with the bandgap widening **(Figure S7b)**. The dynamic of the excited states for the different chloride concentration in $MAPb(Br_{1-x}Cl_x)_3$ has been determined using time-resolved PL in single photon counting mode (TCSPC) **(Figure S7c)**. The PL decay contains two components regardless of the chloride concentration, a fast component ie. faster than 20 ns, ascribed to the carriers filling of the traps and a second-long contribution ascribed to the dynamic of the Shockley-Read-Hall (SRH) recombination. A tail fitting shows that SRH recombination is accelerated upon addition of chloride from 1844 ns, 506 ns, 498 ns, 407 ns to 53 ns for x increasing from 0.00, 0.04, 0.13, 0.20 and 0.26 in $MAPb(Br_{1-x}Cl_x)_3$, respectively. This result points out that excessive concentration of chloride, albeit beneficial from an optical point of view, is detrimental from a photophysical point of view leading to the creation of non-radiative defects and an acceleration of the SRH recombination.
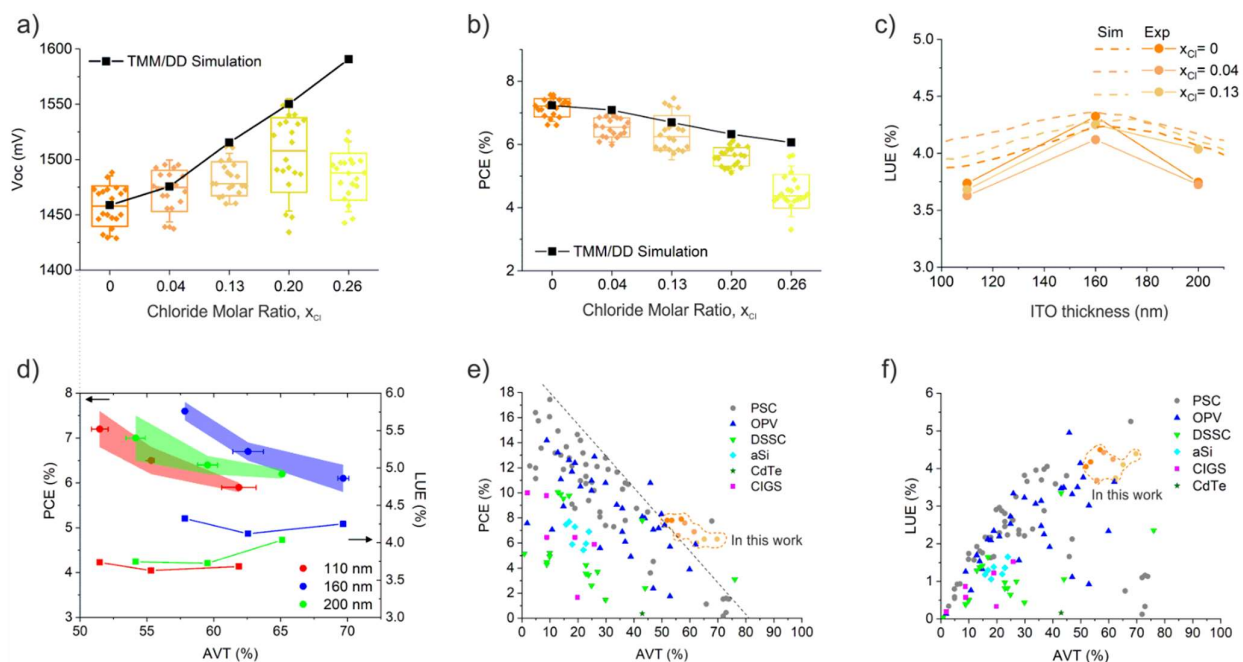
Figure 4. Statistical experimental PV results (box plots) and theoretical TMM/DD results (black dots) by varying the MAPb(Br$_{1-x}$Cl$_x$)$_3$ perovskite compositions (x$_{Cl}$ = 0, 0.04, 0.13, 0.20, 0.26): a) Voc, b) PCE, c) Comparison of the simulated (dashed lines) and experimental (circle dots) LUE results for x$_{Cl}$ = 0, 0.04, 0.13 by varying the ITO thickness. d) PCE (AVT) and LUE (AVT) behaviors obtained by varying the ITO thickness (110nm, 160nm, 200nm) and the perovskite composition (x$_{Cl}$ = 0, 0.04, 0.13). e-f) State of art PCE (AVT) and LUE (AVT) results for TPV technologies (PSC, OPV, DSSC, a-Si, CIGS, CdTe) reported in literature. The orangish circle dots represent our results obtained in this paper for ST-PSC.

Figure 4a-b provides an overview of the theoretical/experimental results on the batches of ST-PSCs for the investigated x$_{Cl}$ molar ratios and t$_{ITO}$ equal to 110nm. The J-V curves under forward and reverse scan directions and the Maximum Power Point Tracking (MPPT) profiles undere AM1.5G 1 Sun illumination conditions are reported in **Figure S8a-b** for the representative ST-PSC devices based on MAPb(Br$_{1-x}$Cl$_x$)$_3$ perovskite compositions. The data show an increase of the average V$_{OC}$ (**Figure 4a**) compared to pure bromide perovskite (x$_{Cl}$ =0) for x$_{Cl}$ =0.04, x$_{Cl}$ =0.13 and x$_{Cl}$ =0.20 in a reasonable agreement with the increase of the optical band gap and the results obtained from TMM/DD simulations (red dotted curve). However, increasing further the x$_{Cl}$ to 0.26 we observed a drastic decrease of V$_{OC}$ compared with the predicted value given from simulations. This can be ascribed to the worsening of the crystal quality and to the increase of the trap-assisted recombination

at the interface between the perovskite and the selective contact layers[45]. Therefore, the maximum V_{OC} value of 1.54V was obtained with $x_{Cl} = 0.20$. These results are quite encouraging considering the replacement of opaque back-electrode (C, Pt and Au) with a transparent ITO electrode[46]. The trend in short-circuit current density (J_{SC}) is quite well predicted by the TMM calculations, showing a linear decrease by increasing the optical bandgap in accordance to the EQE spectra (**Figure S9-S10**), Similarly, the FF behavior is well reproduced by the theoretical predictions (**Figure S11**). The comparison between experimental values of PCE and simulation results reported in **Figure 4b** shows that the gradual inclusion of chloride leads to a linear decrease of the PCE in ST-PSCs. We found only a noticeable mismatch between the theoretical and the experimental results of up to 1% for $x_{Cl} = 0.26$. It is related to the V_{OC} drop observed for $x_{Cl} = 0.26$ (**Figure 4a**) and, to a minor extent, to J_{SC} (**Figure S9**). A batch of eight ST-PSCs was fabricated by varying the t_{ITO} and for the most promising perovskite compositions ($x_{Cl} = 0$, 0.04, 0.13). The average photovoltaic parameters are reported in **Table S3**. As predicted by the simulations (**Figure 3c**), the average PCE is not highly affected by the increase of the t_{ITO} but mainly by the increase of x_{Cl}. However, the decrease in V_{OC} at higher t_{ITO} is well compensated by the increase of the FF parameter (**Figure S12**). The increase of the FF is well explained by the reduction of the series resistance driven by the decrease of the ITO sheet resistance (see **Figure 3b**). The slight decrease in V_{OC} could be due to the sputtering-induced damage of the PTAA polymer after prolonged UV light soaking activated by the Ar^+ plasma [47].

In **Figure 4c**, the experimental LUE parameters are reported by varying the ITO thickness and the perovskite composition (colored circle dots). The dashed line represents the theoretical LUE results extracted from the map reported in **Figure 3f**. The experimental LUEs well reproduced the predicted behavior of the theoretical LUE by varying the t_{ITO} showing a remarkable improvement at $t_{ITO} = 160nm$ for all the $MAPb(Br_{1-x}Cl_x)_3$ perovskite compositions. In **Figure S13**, it is reported the investigation on the relative errors obtained by the comparison of experimental/theoretical values (named as X_{EXP} and X_{SIM}, respectively). The averaged PCE (AVT) behaviors, shown in Figure 4d, further confirm that the ITO thickness controls the AVT of the entire device stack leading to higher

LUE for t_{ITO} = 160nm. Interestingly, a LUE = 4.3 has been reached for x_{Cl} = 0.13 demonstrating the effective role of the chloride inclusion into the perovskite structure. It demonstrates that the development of $MAPb(Br_{1-x}Cl_x)_3$ perovskite absorbers appears beneficial on the design of ST-PSC with AVT approaching 70%. In figure 4e-f, we report the state of art PCE and LUE metrics obtained by several single-junction TPV technologies (PSC, OPV, DSSC, etc.) as function of the corresponding AVT values. Our results highlight that the obtained PCE and LUE values in this work are representing the state of art for TPV technology and can be suitable for the development of PV windows for BIPV.

We evaluated the light stability of a batch of four not encapsulated ST-PSC using x_{Cl} = 0 and 0.13 by performing a light soaking test of 400h at 1 sun illumination condition and under Maximum Power Poin Tracking (MPPT) (**Figure S14**). The results are compared in terms of the t_{80} parameter (Time required to reach 80 % retention of the initial PCE) following the ISOS-L-1 protocol described from Khenkin at al.[48]. The T80 parameters are longer than 200 hours for both ST-PSC batches using x_{Cl} = 0 and x_{Cl} =0.13 demonstrating promising light stability of the $MAPb(Br_{1-x}Cl_x)_3$ perovskite absorbers. The thermal cycling test was also performed by measuring the J-V curves of the ST-PSC (x_{Cl} = 0 and x_{Cl} =0.13) during a heating ramp from 25°C to 85°C and then evaluating the recovery at 25°C after the cooling ramp. In **Figure S15**, the normalized PCE (T) behaviors and the temperature coefficients (γ) are reported. The ST-PSC devices retained the PCE value after cooling down at 25°C without showing any degradation. The ST-PSC devices showed γ values similar to other PV technologies, equal to -0.28%/°C and -0.24%/°C for x_{Cl} = 0 and x_{Cl} =0.13, respectively.

Finally, we investigated the up-scaling process of $MAPb(Br_{1-x}Cl_x)_3$ perovskite by developing Semi-transparent Perovskite Solar Modules (ST-PSM) using the optimized stack for x_{Cl} = 0, 0.04 and 0.13. The layout of the ST-PSM modules was designed starting from our previous works on PSM, where the P1-P2-P3 interconnection permits the serial interconnection between adjacent cells[49-52]. In particular, P2 ablation was performed on $FTO/c-TiO_2/m-TiO_2/MAPb(Br_{1-x}Cl_x)_3/PTAA$ stacks in

order to minimize the contact resistance between the rear ITO and the front FTO electrodes. In **Figure S16a**, we reported the image of several P2 ablations obtained by varying the laser fluence from 155 to 621 mJ·cm^{-2} per pulse. The P1-P2-P3 optimization assisted the development of ST-PSMs with aperture ratio of 91% and aperture areas of 11.35 cm^2 for 5.6×5.6 cm^2 and 53.6 cm^2 for 10×10 cm^2 substrates with interconnection width of 500μm (Figure S15b). In **Figure 5a**, we report the images in transparency of the pure bromide perovskite ($x_{Cl} = 0$) ST-PSC and ST-PSMs with active area of 0.42 cm^2, 10.3 cm^2 and 48.8 cm^2 deposited on 2.5×2.5 cm^2, 5.7×5.7 cm^2 and 10×10 cm^2 glass substrates, respectively. The results show maximum PCEs of 7.1 % for 10.3 cm^2 and 6.1% for 48.8 cm^2-sized modules using MAPbBr$_3$ perovskite ($x_{Cl} = 0$). Negligible J-V hysteresis was measured for ST-PSMs confirming the same trend shown for ST-PSC cells. To better understand the results obtained from the up-scaling process, we compared the J-V between single cell and individual cells of the modules (**Figure S17**). For modules, the J-V of the individual cell is deduced by the hypothesis that all the constituent cells give the same contribution in Voc. Then, the Voc of the modules are divided by the number of the constituent cells (n) being equal to 5 and 13 for 10.3 cm^2 and 48.8 cm^2 active areas, respectively. Interestingly, the Voc/n is not influenced during the up-scaling process, being equal to 1.51 V and 1.47 V for 10.3 cm^2 and 48.8 cm^2-sized modules, respectively. Unfortunately, the Jsc value slightly decreased for 48.8 cm^2-sized ST-PSM mainly due to current mismatch between the constituent cells forming the module. This is mainly ascribed to the lack in uniformity of the MAPbBr$_3$ perovskite after the methylamine post-treatment. The optimized up-scaling process was then applied on modules based on MAPb(Br$_{1-x}$Cl$_x$)$_3$ perovskite using $x_{Cl} = 0.04$ and $x_{Cl} = 0.13$. The J-V results (**Figure 5d**) confirm negligible J-V hysteresis also deduced from stable MPP tracking shown in the inset figure for all the perovskite composition. Interestingly, high Voc/cell (>1.52 V) and FF (>70%) have been demonstrated for $x_{Cl} = 0.13$ reaching steady state PCE values above 6.1%. The average photovoltaic parameters obtained in a batch of four modules for each MAPb(Br$_{1-x}$Cl$_x$)$_3$ are reported in **Table 2**.

Table 2. Averaged photovoltaic parameters of 10.3 cm^2-sized ST-PSM by varying the MAPb(Br$_{1-x}$Cl$_x$)$_3$ perovskite composition.

MAPb(Br$_{1-x}$Cl$_x$)$_3$	Voc (V)	Isc (mA)	FF (%)	PCE (%)
x$_{Cl}$ = 0	7.31 ± 0.12	-13.87 ± 0.44	68.05 ± 3.24	6.67 ± 0.28
x$_{Cl}$ = 0.04	7.35 ± 0.11	-13.15 ± 0.61	63.86 ± 0.93	5.96 ± 0.37
x$_{Cl}$ = 0.13	7.79 ± 0.08	-11.85 ± 0.40	70.17 ± 1.64	6.26 ± 0.20

The electroluminescence (EL) mapping reported in **Figure 5c** confirms that the 10.3 cm^2-sized module demonstrated good uniformity of the device stack for both x$_{Cl}$ = 0 and x$_{Cl}$ = 0.13. Instead, the x$_{Cl}$ = 0.04 sample showed less EL map uniformity in agreement with the detrimental results obtained in terms of Voc and FF (see Table 2). However, despite a larger level of inhomogeneity, the x$_{Cl}$ = 0.04 device still exhibits remarkably higher average EL intensity with rapid increase at increased voltage. This indicates that, on average, less non-radiative recombinations occur with respect to the other x$_{Cl}$ composition (**Figure S18**). Further evidences are deduced by analyzing the transfer function which depicts the ability of the devices to locally increase the EL and therefore the current at a certain pixel (x,y), when additional voltage is settled at the terminals [53]. The low transfer function of the x$_{Cl}$ = 0.04 device suggests limited current extraction resulting in higher EL intensity (i.e. high local voltage). Instead, the x$_{Cl}$=0.13 device shows the highest transfer function, which means that the current transport at this voltage is more efficient as confirmed from the higher FF, reflecting a lower series resistance. Furthermore, no failure in P1-P2-P3 process is expected by the analysis of the EL map uniformity close to the interconnection areas. The cross profiles are depicted in **Figure S19**. Thanks to the enhanced AVT value, the MAPb(Br$_{1-x}$Cl$_x$)$_3$ stack for x$_{Cl}$ = 0.13 is chosen for the fabrication of larger PSMs on 10x10 cm^2 substrates. Promising results were obtained showing the following photovoltaic parameters under reverse scan direction: Voc = 20.06 V (1.54 V/Cell), Isc = 19.42 mA, FF = 69.22% and PCE equal to 5.54% and tracked PCE after MPPT of 60s equal to 5.30%. The visible transmittance spectrum of the ST-PSM for x$_{Cl}$ = 0.13 is reported in **Figure S20** showing

an AVT value of 59.4%, in good agreement with the results obtained for t_{ITO} equal to 110nm. Interestingly, the PV performance losses were minimized during the up-scaling process showing only 13% relative decrease between the PCE measured on 0.4cm^2 sized ST-PSC (6.3%) and 48.8 cm^2-sized ST-PSM (5.54%) for x_{Cl} = 0.13. Our results are comparable with the PV performance losses shown in state-of-art opaque PSM fabricated on similar substrate size [54-56].

The not-encapsulated ST-PSM module was further monitored under shelf-life conditions for 2400 hours without showing significant decrease in PCE. **Figure 5f-g** show the results on PCE (AVT) and LUE (AVT) achieved by the TPV technologies (PSC, OPV, DSSC and a:Si) regarding the development of semi-transparent mini-modules. In our knowledge, our results represent the state-of-art for semi-transparent PV modules showing outstanding LUE values with AVT greater than 50%.
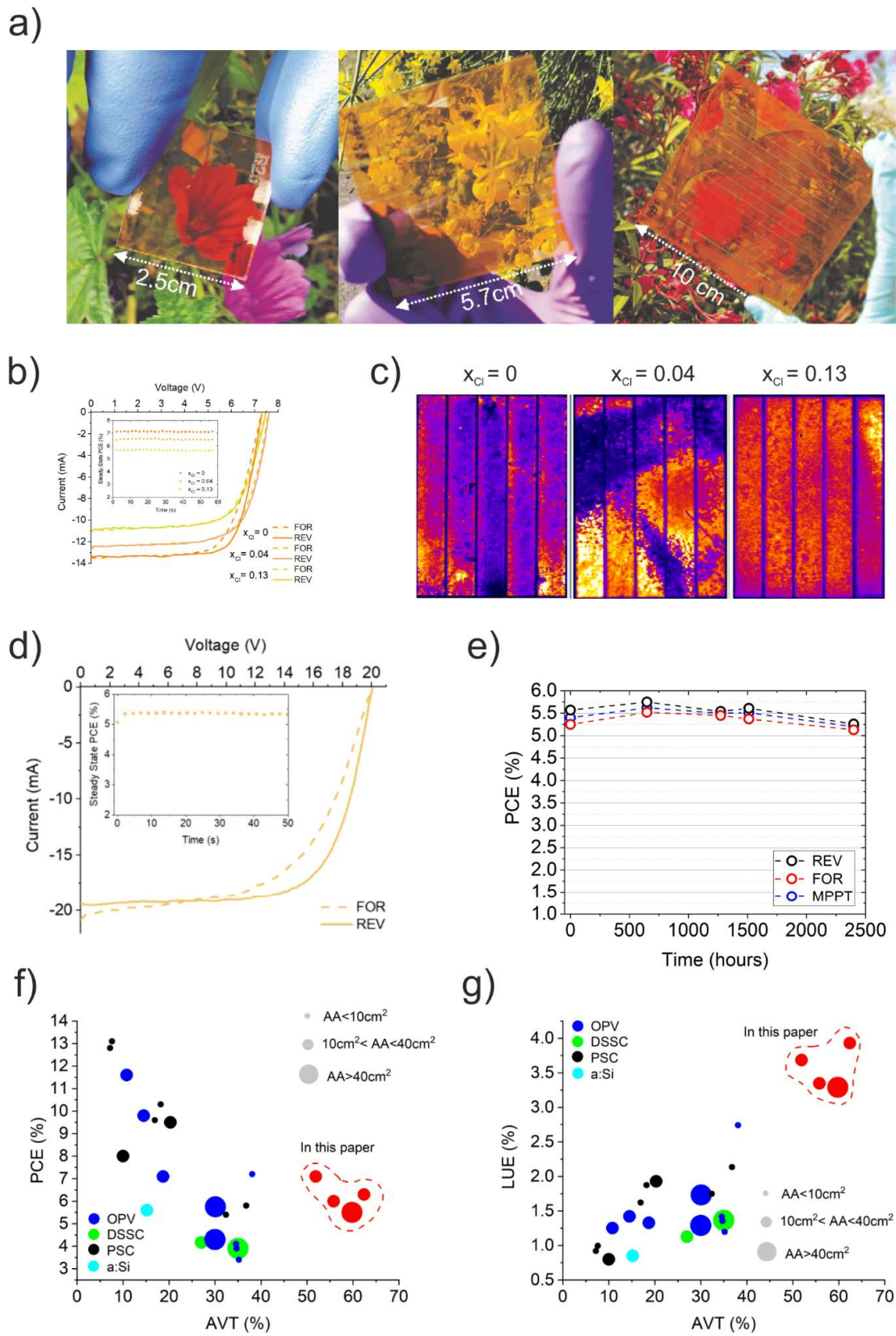
Figure 5. a) Pictures of the devices fabricated during the up-scaling process of MAPb(Br$_{1-x}$Cl$_x$)$_3$ stack. The substrate sizes are 2.5cm x 2.5cm^2 for ST-PSC with active area of 0.4 cm^2, 5.7cmx5.7cm

for ST-PSM with active area of 10.3 cm^2 and 10cm x 10cm for ST-PSM with active area of 48.8cm^2. b) J-V characteristics of 10.3 cm^2-sized ST-PSM (x_{Cl} =0, 0.04, 0.13) measured under reverse and forward scan direction (AM1.5G 1 Sun illumination conditions). The inset graph shows the steady-state PCE behavior at MPPT polarization. c) EL maps of 10.3 cm^2-sized ST-PSM (x_{Cl}=0, 0.04, 0.13). d) J-V characteristics of 48.8 cm^2-sized ST-PSM (x_{Cl} = 0.13) measured under reverse and forward scan direction (AM1.5G 1 Sun illumination conditions). The inset graph shows the steady-state PCE behavior at MPPT polarization. e) PCE of the 48.8 cm^2-sized ST-PSM (x_{Cl} = 0.13) measured during the shelf-life test of 2400 hours under reverse/forward scan directions and MPPT polarization. For MPPT polarization, each point refers to the measure of the steady state PCE after 60 seconds of MPPT. f-g) PCE (AVT) (f) and LUE (AVT) (g) results for semi-transparent mini-modules made by different TPV technologies. The active area (AA) of the modules is also considered by varying the size of the dot (small, AA is lower than 10cm^2; medium, AA is in between of 10cm^2 and 40cm^2; large: AA is larger than 40cm^2)

CONCLUSION

In conclusion, we have reported the development of highly efficient semi-transparent Perovskite Solar Cells and Modules, tailored by combining theoretical calculation and experimental demonstration. The device stack optimization involves the development of a class of MAPb(Br$_{1-x}$Cl$_x$)$_3$ perovskite absorbers that have been characterized in terms of optical, morphological and structural properties. The absorption coefficient of MAPb(Br$_{1-x}$Cl$_x$)$_3$ perovskite are then transferred as input for optical simulations using TMM method in order to evaluate the potential of this class of perovskite absorbers for BIPV application. TMM method gives us multiple outputs such as: the transmittance/reflectance and AVT of the stack, the thickness of the constituent layers and finally the generation profile needed to for the Drift Diffusion simulation tool. The combined TMM/DD simulative approach has been validated showing perfect matching with the experimental results. Furthermore, we found that the AVT of the device stack can be further enhanced by varying the thickness of the ITO electrode without impacting on the photovoltaic performance. Both theoretical and experimental results confirmed that the use of MAPb(Br$_{1-x}$Cl$_x$)$_3$ perovskite composition at specific chloride molar ratios (0.04 and 0.13) improves the TPV metrics (AVT and LUE). The best results are obtained for a chloride molar ratio equal to 0.13, showing a PCE of 6.3%, an average AVT of 69.7% corresponding

to a LUE of 4.37%. Moreover, we evaluated the light stability and thermal cycling of not-encapsulated devices showing very promising results in terms of T80 (> 200h) and temperature coefficients (0.24%/°C for x_{Cl} = 0.13). Finally, we evaluated the up-scaling process of perovskite solar modules on substrates with active area of 10 cm^2 using MAPb(Br$_{1-x}$Cl$_x$)$_3$ perovskite with x_{Cl} = 0, 0.04, 0.13. The results show average PCEs being equal to 6.67 ± 0.28 %, 5.96 ± 0.37 % and 6.26 ± 0.20 %, respectively. For x_{Cl} = 0.13, we further demonstrated the fabrication of semi-transparent PSM with active area of 48 cm^2 showing a PCE equal to 5.45%, AVT equal to 59.4% and shelf-life stability longer than 2400 hours. The results shown in this study represent the state of art for TPV technologies with AVT greater than 50% suitable for the development of PV windows in BIPV field.

Acknowledgments

References

[1] M. Green, E. Dunlop, J. Hohl-Ebinger, M. Yoshita, N. Kopidakis, X. Hao, Progress in Photovoltaics: Research and Applications, 29 (2021) 3-15.

[2] O. Almora, D. Baran, G.C. Bazan, C. Berger, C.I. Cabrera, K.R. Catchpole, S. Erten-Ela, F. Guo, J. Hauch, A.W.Y. Ho-Baillie, T.J. Jacobsson, R.A.J. Janssen, T. Kirchartz, N. Kopidakis, Y. Li, M.A. Loi, R.R. Lunt, X. Mathew, M.D. McGehee, J. Min, D.B. Mitzi, M.K. Nazeeruddin, J. Nelson, A.F. Nogueira, U.W. Paetzold, N.G. Park, B.P. Rand, U. Rau, H.J. Snaith, E. Unger, L. Vaillant-Roca, H.L. Yip, C.J. Brabec, Advanced Energy Materials, 11 (2021).

[3] D.-J. van de Ven, I. Capellan-Peréz, I. Arto, I. Cazcarro, C. de Castro, P. Patel, M. Gonzalez-Eguino, Scientific Reports, 11 (2021) 2907.

[4] W. Wei, H.M. Skye, Renewable and Sustainable Energy Reviews, 142 (2021).

[5] C.J. Traverse, R. Pandey, M.C. Barr, R.R. Lunt, Nature Energy, 2 (2017) 849-860.

[6] F. Guo, X. Zhu, K. Forberich, J. Krantz, T. Stubhan, M. Salinas, M. Halik, S. Spallek, B. Butz, E. Spiecker, T. Ameri, N. Li, P. Kubis, D.M. Guldi, G.J. Matt, C.J. Brabec, Advanced Energy Materials, 3 (2013) 1062-1067.

[7] J. Krantz, T. Stubhan, M. Richter, S. Spallek, I. Litzov, G.J. Matt, E. Spiecker, C.J. Brabec, Advanced Functional Materials, 23 (2013) 1711-1717.

[8] Q. Xue, R. Xia, C.J. Brabec, H.L. Yip, Energy and Environmental Science, 11 (2018) 1688-1709.

[9] X. Wang, J. Wang, J. Han, D. Huang, P. Wang, L. Zhou, C. Yang, X. Bao, R. Yang, Nano Energy, 81 (2021) 105612.

[10] P. Mariani, L. Vesce, A. Di Carlo, Semiconductor Science and Technology, 30 (2015).

[11] D. Colonna, S. Colodrero, H. Lindström, A. Di Carlo, H. Míguez, Energy and Environmental Science, 5 (2012) 8238-8243.

[12] B. O'Regan, M. Grätzel, Nature, 353 (1991) 737-740.

[13] A. Hagfeldt, G. Boschloo, L. Sun, L. Kloo, H. Pettersson, Chemical Reviews, 110 (2010) 6595-6663.

[14] W. Naim, V. Novelli, I. Nikolinakos, N. Barbero, I. Dzeba, F. Grifoni, Y. Ren, T. Alnasser, A. Velardo, R. Borrelli, S. Haacke, S.M. Zakeeruddin, M. Graetzel, C. Barolo, F. Sauvage, JACS Au, 1 (2021) 409-426.

[15] H. Min, D.Y. Lee, J. Kim, G. Kim, K.S. Lee, J. Kim, M.J. Paik, Y.K. Kim, K.S. Kim, M.G. Kim, T.J. Shin, S. Il Seok, Nature, 598 (2021) 444-450.

[16] A. Al-Ashouri, E. Köhnen, B. Li, A. Magomedov, H. Hempel, P. Caprioglio, J.A. Márquez, A.B.M. Vilches, E. Kasparavicius, J.A. Smith, N. Phung, D. Menzel, M. Grischek, L. Kegelmann, D. Skroblin, C. Gollwitzer, T. Malinauskas, M. Jošt, G. Matič, B. Rech, R. Schlatmann, M. Topič, L.

Korte, A. Abate, B. Stannowski, D. Neher, M. Stolterfoht, T. Unold, V. Getautis, S. Albrecht, Science, 370 (2020) 1300-1309.

[17] K.A. Bush, A.F. Palmstrom, Z.J. Yu, M. Boccard, R. Cheacharoen, J.P. Mailoa, D.P. McMeekin, R.L.Z. Hoye, C.D. Bailie, T. Leijtens, I.M. Peters, M.C. Minichetti, N. Rolston, R. Prasanna, S. Sofia, D. Harwood, W. Ma, F. Moghadam, H.J. Snaith, T. Buonassisi, Z.C. Holman, S.F. Bent, M.D. McGehee, Nature Energy, 2 (2017).

[18] D.P. McMeekin, G. Sadoughi, W. Rehman, G.E. Eperon, M. Saliba, M.T. Hörantner, A. Haghighirad, N. Sakai, L. Korte, B. Rech, M.B. Johnston, L.M. Herz, H.J. Snaith, Science, 351 (2016) 151-155.

[19] F. Sahli, J. Werner, B.A. Kamino, M. Bräuninger, R. Monnard, B. Paviet-Salomon, L. Barraud, L. Ding, J.J. Diaz Leon, D. Sacchetto, G. Cattaneo, M. Despeisse, M. Boccard, S. Nicolay, Q. Jeangros, B. Niesen, C. Ballif, Nature Materials, 17 (2018) 820-826.

[20] M. Saliba, T. Matsui, J.Y. Seo, K. Domanski, J.P. Correa-Baena, M.K. Nazeeruddin, S.M. Zakeeruddin, W. Tress, A. Abate, A. Hagfeldt, M. Grätzel, Energy and Environmental Science, 9 (2016) 1989-1997.

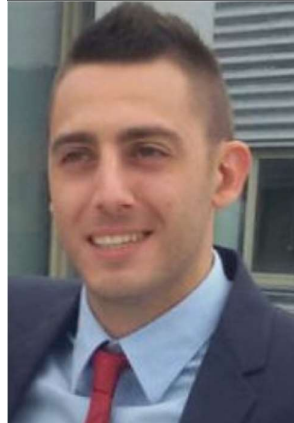[21] T. Singh, T. Miyasaka, Advanced Energy Materials, 8 (2018).

[22] L. Schmidt-Mende, V. Dyakonov, S. Olthof, F. Ünlü, K.M.T. Lê, S. Mathur, A.D. Karabanov, D.C. Lupascu, L.M. Herz, A. Hinderhofer, F. Schreiber, A. Chernikov, D.A. Egger, O. Shargaieva, C. Cocchi, E. Unger, M. Saliba, M.M. Byranvand, M. Kroll, F. Nehm, K. Leo, A. Redinger, J. Höcker, T. Kirchartz, J. Warby, E. Gutierrez-Partida, D. Neher, M. Stolterfoht, U. Würfel, M. Unmüssig, J. Herterich, C. Baretzky, J. Mohanraj, M. Thelakkat, C. Maheu, W. Jaegermann, T. Mayer, J. Rieger, T. Fauster, D. Niesner, F. Yang, S. Albrecht, T. Riedl, A. Fakharuddin, M. Vasilopoulou, Y. Vaynzof, D. Moia, J. Maier, M. Franckevičius, V. Gulbinas, R.A. Kerner, L. Zhao, B.P. Rand, N. Glück, T. Bein, F. Matteocci, L.A. Castriotta, A. Di Carlo, M. Scheffler, C. Draxl, APL Materials, 9 (2021) 109202.

[23] C. Roldán-Carmona, O. Malinkiewicz, R. Betancur, G. Longo, C. Momblona, F. Jaramillo, L. Camacho, H.J. Bolink, Energy & Environmental Science, 7 (2014) 2968-2973.

[24] M.B. Upama, M.A. Mahmud, H. Yi, N.K. Elumalai, G. Conibeer, D. Wang, C. Xu, A. Uddin, Organic Electronics, 65 (2019) 401-411.

[25] L. Yuan, Z. Wang, R. Duan, P. Huang, K. Zhang, Q. Chen, N.K. Allam, Y. Zhou, B. Song, Y. Li, Journal of Materials Chemistry A, 6 (2018) 19696-19702.

[26] D. Marongiu, S. Lai, V. Sarritzu, E. Pinna, G. Mula, M.L. Mercuri, M. Saba, F. Quochi, A. Mura, G. Bongiovanni, ACS Applied Materials & Interfaces, 11 (2019) 10021-10027.

[27] L. Zhang, M.T. Hörantner, W. Zhang, Q. Yan, H.J. Snaith, Solar Energy Materials and Solar Cells, 160 (2017) 193-202.

[28] T. Jesper Jacobsson, J.-P. Correa-Baena, M. Pazoki, M. Saliba, K. Schenk, M. Grätzel, A. Hagfeldt, Energy & Environmental Science, 9 (2016) 1706-1724.

[29] G.E. Eperon, V.M. Burlakov, A. Goriely, H.J. Snaith, ACS Nano, 8 (2014) 591-598.

[30] A. Sadhanala, F. Deschler, T.H. Thomas, S.E. Dutton, K.C. Goedel, F.C. Hanusch, M.L. Lai, U. Steiner, T. Bein, P. Docampo, D. Cahen, R.H. Friend, The Journal of Physical Chemistry Letters, 5 (2014) 2501-2505.

[31] R. Comin, G. Walters, E.S. Thibau, O. Voznyy, Z.-H. Lu, E.H. Sargent, Journal of Materials Chemistry C, 3 (2015) 8839-8843.

[32] N. Arora, M.I. Dar, M. Abdi-Jalebi, F. Giordano, N. Pellet, G. Jacopin, R.H. Friend, S.M. Zakeeruddin, M. Grätzel, Nano Letters, 16 (2016) 7155-7162.

[33] F.C. Hanusch, E. Wiesenmayer, E. Mankel, A. Binek, P. Angloher, C. Fraunhofer, N. Giesbrecht, J.M. Feckl, W. Jaegermann, D. Johrendt, T. Bein, P. Docampo, The Journal of Physical Chemistry Letters, 5 (2014) 2791-2795.

[34] L. Zuo, X. Shi, W. Fu, A.K.Y. Jen, Advanced Materials, 31 (2019) 1901683.

[35] D. Liu, C. Yang, R.R. Lunt, Joule, 2 (2018) 1827-1837.

[36] R.J. Elliott, Physical Review, 108 (1957) 1384-1389.

[37] Y. Yang, M. Yang, K. Zhu, J.C. Johnson, J.J. Berry, J. van de Lagemaat, M.C. Beard, Nature Communications, 7 (2016) 12613.

[38] F. Mariano, A. Cretì, L. Carbone, A. Genco, S. D'Agostino, S. Carallo, G. Montagna, M. Lomascolo, M. Mazzeo, Communications Physics, 3 (2020) 41.

[39] X. Chen, H. Lu, Y. Yang, M.C. Beard, The Journal of Physical Chemistry Letters, 9 (2018) 2595-2603.

[40] A. Singh, F. Matteocci, H. Zhu, D. Rossi, S. Mejaouri, S. Cacovich, M. Auf Der Maur, F. Sauvage, A. Gagliardi, M. Grätzel, A. Di Carlo, Solar RRL, n/a (2021).

[41] M.C. Troparevsky, A.S. Sabau, A.R. Lupini, Z. Zhang, Opt. Express, 18 (2010) 24715-24721.

[42] M.A.d. Maur, G. Penazzi, G. Romano, F. Sacconi, A. Pecchia, A.D. Carlo, IEEE Transactions on Electron Devices, 58 (2011) 1425-1432.

[43] A. Hernández-Granados, A.N. Corpus-Mendoza, P.M. Moreno-Romero, C.A. Rodríguez-Castañeda, J.E. Pascoe-Sussoni, O.A. Castelo-González, E.C. Menchaca-Campos, J. Escorcia-García, H. Hu, Optical Materials, 88 (2019) 695-703.

[44] E. Lamanna, F. Matteocci, E. Calabrò, L. Serenelli, E. Salza, L. Martini, F. Menchini, M. Izzi, A. Agresti, S. Pescetelli, S. Bellani, A.E. Del Río Castillo, F. Bonaccorso, M. Tucci, A. Di Carlo, Joule, 4 (2020) 865-881.

[45] A. Zohar, M. Kulbak, I. Levine, G. Hodes, A. Kahn, D. Cahen, ACS Energy Letters, 4 (2019) 1-7.

[46] N. Kedem, M. Kulbak, T.M. Brenner, G. Hodes, D. Cahen, Physical Chemistry Chemical Physics, 19 (2017) 5753-5762.

[47] Z. Bagheri, F. Matteocci, E. Lamanna, D. Di Girolamo, A.G. Marrani, R. Zanoni, A. Di Carlo, A. Moshaii, Solar Energy Materials and Solar Cells, 215 (2020) 110606.

[48] M.V. Khenkin, E.A. Katz, A. Abate, G. Bardizza, J.J. Berry, C. Brabec, F. Brunetti, V. Bulović, Q. Burlingame, A. Di Carlo, R. Cheacharoen, Y.-B. Cheng, A. Colsmann, S. Cros, K. Domanski, M. Dusza, C.J. Fell, S.R. Forrest, Y. Galagan, D. Di Girolamo, M. Grätzel, A. Hagfeldt, E. von Hauff,

H. Hoppe, J. Kettle, H. Köbler, M.S. Leite, S. Liu, Y.-L. Loo, J.M. Luther, C.-Q. Ma, M. Madsen, M. Manceau, M. Matheron, M. McGehee, R. Meitzner, M.K. Nazeeruddin, A.F. Nogueira, Ç. Odabaşı, A. Osherov, N.-G. Park, M.O. Reese, F. De Rossi, M. Saliba, U.S. Schubert, H.J. Snaith, S.D. Stranks, W. Tress, P.A. Troshin, V. Turkovic, S. Veenstra, I. Visoly-Fisher, A. Walsh, T. Watson, H. Xie, R. Yıldırım, S.M. Zakeeruddin, K. Zhu, M. Lira-Cantu, Nature Energy, 5 (2020) 35-49.

[49] A.L. Palma, F. Matteocci, A. Agresti, S. Pescetelli, E. Calabrò, L. Vesce, S. Christiansen, M. Schmidt, A.D. Carlo, IEEE Journal of Photovoltaics, 7 (2017) 1674-1680.

[50] F. Matteocci, L. Vesce, F.U. Kosasih, L.A. Castriotta, S. Cacovich, A.L. Palma, G. Divitini, C. Ducati, A. Di Carlo, ACS Applied Materials & Interfaces, 11 (2019) 25195-25204.

[51] F. Di Giacomo, L.A. Castriotta, F.U. Kosasih, D. Di Girolamo, C. Ducati, A. Di Carlo, Micromachines, 11 (2020).

[52] L. Vesce, M. Stefanelli, F. Matteocci, L.A. Castriotta, E. Lamanna, J. Herterich, F.D. Giacomo, M. Kohlstädt, U. Würfel, A.D. Carlo, 2020 AEIT International Annual Conference (AEIT)2020, pp. 1-5.

[53] J. Wong, M.A. Green, Physical Review B, 85 (2012) 235205.

[54] Y. Ding, B. Ding, H. Kanda, O.J. Usiobo, T. Gallet, Z. Yang, Y. Liu, H. Huang, J. Sheng, C. Liu, Y. Yang, V.I.E. Queloz, X. Zhang, J.-N. Audinot, A. Redinger, W. Dang, E. Mosconic, W. Luo, F. De Angelis, M. Wang, P. Dörflinger, M. Armer, V. Schmid, R. Wang, K.G. Brooks, J. Wu, V. Dyakonov, G. Yang, S. Dai, P.J. Dyson, M.K. Nazeeruddin, Nature Nanotechnology, 17 (2022) 598-605.

[55] S. Chen, X. Dai, S. Xu, H. Jiao, L. Zhao, J. Huang, Science, 373 (2021) 902-907.

[56] L.A. Castriotta, M. Zendehdel, N. Yaghoobi Nia, E. Leonardi, M. Löffler, B. Paci, A. Generosi, B. Rellinghaus, A. Di Carlo, Advanced Energy Materials, 12 (2022) 2103420.

Vitae

	Fabio Matteocci received his MSc degree in Electrical Engineering from the University of Rome "Tor Vergata" (UTV) in Rome. During his Ph.D. in Electrical Engineering from the Center for Hybrid and Organic Solar Energy (CHOSE) in 2014. He is working on the development of manufacturing process for perovskite solar cell and modules. on the stability of PSCs under moisture, heat and light stresses. Since 2016, he is an Assistant Professor in UTV working on perovskite solar modules, perovskite/c-Si Tandem and photodetectors. He published more than 65 research publications on this topic, with a h-index of 28.
	Daniele Rossi received the master's degree in 2015 and the Ph.D. degree in 2019 in Electronics Engineering from the University of Rome Tor Vergata. Since 2019 takes up a Post Doc position within the OLAB (Optoelectronic and Nanoelectronic Devices) research group of Electronics Engineering Department at University of Rome Tor Vergata. His work focuses on organic electronics and simulation of optoelectronic devices, in particular perovskite solar cells and OLEDs.
	Luigi Angelo Castriotta got in 2021 his Ph.D. in Electronics Engineering from TorVergata University (Italy) as a Marie-Curie Fellow as part of the ITN MAESTRO; He got his bachelor's degree in chemistry at the same University and Masters' in "Nanoscience and Nanotechnology" at UB(Spain) and in "Organic Molecular Electronics" at TUD (Germany). Currently, he works as a post-Doctoral fellow in collaboration with ENEA, focusing on flexible single-junction perovskite solar cells and modules. In 2023 he'll join Prof. Huang's group at the UNC (US), as a Global Marie-Curie Post-Doctoral Fellow, following his work on Perovskite-based solar device upscaling on flexible substrate.
	Daniel Ory received his Phd in Physics from University Paris Sciences & Lettres in 2021. He was also graduated in Mechanical Engineering in 1992. After an extensive carrier in automotive industry, he became a researcher in the field of photovoltaic energy within Electricité de France (EDF), one of the biggest electricity utility worldwide. His research activity focuses on the luminescence properties of semi-conductors and related optical characterizations.

	Salim Mejaouri graduated in materials science from INSA Lyon, France in 2017 with a double degree in mechanical engineering from University of Sherbrooke, Canada. There, he developed a MEMS-based device able to perform neuromorphic computing. In 2018, he joined the IPVF as a research engineer and he implemented a laser-based interconnection process for perovskite modules. He started his PhD in December 2019 on degradation mechanisms in perovskite solar cells under environmental stresses. He aims at understanding these phenomena with correlative characterization techniques based on electronic microscopy.
	M. Auf der Maur is associate Professor with the Department of Electronic Engineering of the University of Rome Tor Vergata. He received his M.Sc in 2004 from ETH Zurich and his PhD in 2008 from University of Rome Tor Vergata. His current research interest is in optical and electrical modelling of solar cells and LEDs (halide perovskites, III-nitrides and III-V) and in development of multiscale/multiphysics simulation models.
	Frédéric Sauvage is currently research director at CNRS and group leader at the LCRS. He obtained his Ph.D. in 2006 under the supervision of Prof. Tarascon, post-doctoral fellow at Northwestern University (Prof. Poeppelmeir) and joined the Swiss Federal Institute of Technology within the group of Prof. Gräetzel. His research interest is on stability of dye-sensitized solar cells and perovskite solar cells, developed the concept of the transparent and colorless dye-sensitized solar cells based on wavelength selective NIR sensitization. He has published >90 peer-review articles, inventor of 8 patents and coordinator of the Impressive project funded by the EC.
	Stefania Cacovich is a Marie Curie Individual Fellow in Physics at CNRS. She holds a Bachelor degree in Industrial Engineering and a Master degree in Materials and Process Engineering from the University of Trieste (Italy). She received her PhD in Materials Science from the University of Cambridge (UK) in 2018. Her research activity lies in the field of the advanced characterization of hybrid and inorganic materials for photovoltaic applications. Currently, she is focussing on the study of the optoelectronic and transport properties of halide perovskites via multidimensional luminescence imaging.
	Aldo Di Carlo is head of the Institute for Structure of the Matter of the Italian National Research Council (CNR-ISM), full professor at the University of Rome "Tor Vergata" (Italy) and visiting professor at the National University of Science and Technology MISIS of Moscow (Russia). He founded the Center for Hybrid and Organic Solar Energy (CHOSE) which

involves more than 30 researchers for the development and industrialization of the organic and hybrid organic/inorganic photovoltaic technologies. Di Carlo is author/coauthor of more than 500 scientific publications on international journals, 13 patents and several book chapters.